












## Proton and neutron contributions to the quadrupole transition strengths in $^{39}\text{Ca}$ and $^{39}\text{K}$ studied by lifetime measurements of mirror transitions

A. Sanchez <sup>1,2,\*</sup>, H. Iwasaki <sup>1,2,†</sup>, A. Revel <sup>1,2</sup>, B. A. Brown <sup>1,2</sup>, J. Ash<sup>1,2</sup>, D. Bazin <sup>1,2</sup>, J. Chen,<sup>1</sup> R. Elder,<sup>1,2</sup> A. Gade <sup>1,2</sup>, A. Goldkuhle,<sup>3</sup> M. Grinder <sup>1,2</sup>, D. Lempke <sup>1,2</sup>, J. Li,<sup>1</sup> B. Longfellow,<sup>1,2,‡</sup> C. Müller-Gatermann <sup>3,4</sup>, J. Pereira,<sup>1</sup> D. Rhodes,<sup>1,2,‡</sup> R. Salinas <sup>1,2</sup> and D. Weisshaar <sup>1</sup>

<sup>1</sup>*Facility for Rare Isotope Beams, Michigan State University, East Lansing, Michigan 48824, USA*

<sup>2</sup>*Department of Physics and Astronomy, Michigan State University, East Lansing, Michigan 48824, USA*

<sup>3</sup>*Institut für Kernphysik der Universität zu Köln, D-50937 Köln, Germany*

<sup>4</sup>*Physics Division, Argonne National Laboratory, Lemont, Illinois 60439, USA*



(Received 29 May 2024; accepted 8 August 2024; published 28 August 2024)

The  $E2$  transition matrix elements of isobaric multiplets are expected to follow a linear trend as a function of isospin projection. However, measurements of the  $2^+ \rightarrow 0^+$  transitions in the  $A = 38$  triplet of Ca, K, and Ar show a deviation from this trend with an enhanced transition strength in  $^{38}\text{Ca}$  with respect to its mirror  $^{38}\text{Ar}$ . We have studied analogue  $11/2^- \rightarrow 7/2^-$   $E2$  transitions in  $^{39}\text{Ca}$  and its mirror partner  $^{39}\text{K}$  to determine if this enhancement persists in neighboring Ca isotopes. Recoil-distance lifetime measurements of  $^{39}\text{Ca}$  and  $^{39}\text{K}$  were performed utilizing a  $^{42}\text{Sc}$  secondary beam, the TRIPLEX plunger, the GRETINA array, and the S800 spectrograph. Our data provide a lifetime measurement of the  $(11/2^-)$  state in  $^{39}\text{Ca}$  as well as an improved lifetime result for the  $(9/2^-)$  state, while the  $^{39}\text{K}$  data are used to validate the present analysis. A comparison of the present data to shell-model calculations suggests an enhanced transition strength in  $^{39}\text{Ca}$ , pointing to both proton and neutron contributions to core excitations across the  $Z = N = 20$  shell gaps in close proximity to  $^{40}\text{Ca}$ .

DOI: [10.1103/PhysRevC.110.024322](https://doi.org/10.1103/PhysRevC.110.024322)

### I. INTRODUCTION

The doubly magic  $Z = N = 20$  region of the nuclear landscape serves as a rich testing ground for isospin symmetry and symmetry-breaking phenomena [1–5]. In the isospin formalism, neutrons and protons are considered two states of the same particle with different isospin projections  $T_z$  due to conservation of isospin in the strong interaction. When this formalism holds, we expect mirror nuclei to have similar level schemes with mirror energy differences typically on the order of 10–100 keV [6]. But when significant discrepancies occur in transition strengths of mirror nuclei, unique opportunities may arise to examine isospin properties and investigate the underlying mechanisms which account for isospin symmetry breaking [4,5,7,8].

Previous work has formulated that the proton matrix elements  $M_p$  for the  $2^+ \rightarrow 0^+$   $E2$  transitions [ $M_p(E2)$ ] of  $T = 1$  isobaric triplets should follow a linear trend as a function of isospin projection  $T_z$  [3]. While this trend holds over a wide mass range, a notable deviation has been observed in the  $A = 38$  triplet of Ca, K, and Ar [4,5]. Cottle *et al.* [4] observed a significant enhancement in the  $^{38}\text{Ca}$  matrix element, deviating from the trend set by the  $^{38}\text{Ar}$  and  $^{38}\text{K}$  matrix elements and therefore hinting at symmetry breaking. But the

authors noted that a more precise measurement of  $^{38}\text{K}$  would strengthen their argument. The call for a better measurement of the  $T = 1, 2^+ \rightarrow 0^+$  transition in  $^{38}\text{K}$  was answered by Estevez *et al.* [5] who demonstrated that the  $^{38}\text{Ca}$  matrix element was indeed larger than predicted based on their improved data on  $^{38}\text{K}$  and shell-model calculations, furthering interest in the  $A = 38$  anomaly.

Recent examination has demonstrated that the ground states of  $^{36}\text{Ca}$  and  $^{38}\text{Ca}$  require proton excitations into the  $fp$  shells to explain the observed  $B(E2; 0^+ \rightarrow 2^+)$  transition strengths [9] and the cross-section ratio  $\sigma(2^+)/\sigma(0^+)$  of  $^{36}\text{Ca}$  measured in the  $2n$  removal reaction from  $^{38}\text{Ca}$  [10]. Dronchi *et al.* [9] concluded that a fraction of proton closed-shell configurations as low as 50% best replicates the  $B(E2; 2^+ \rightarrow 0^+)$  for both  $^{36,38}\text{Ca}$ , which is reinforced by the results of Beck *et al.* [10]. Naturally, the enhancement of the proton matrix elements of  $^{36,38}\text{Ca}$  motivates the study of neighboring Ca isotopes to determine if this enhancement persists. Furthermore, since mirror transitions can be effectively used to study the isospin decomposition of transition strengths [3], here we examine  $^{39}\text{Ca}$  and  $^{39}\text{K}$  mirror nuclei to understand the relative importance of proton and neutron contributions to core excitations in the vicinity of doubly magic  $^{40}\text{Ca}$ .

In the present study, we determine the  $B(E2)$  value for the  $11/2^- \rightarrow 7/2^-$  transitions in  $^{39}\text{Ca}$  and  $^{39}\text{K}$  mirror nuclei via lifetime measurements. We employed the recoil distance method (RDM), utilizing a combination of the A1900 fragment separator [11], the TRIPLEX plunger [12], the GRETINA array [13,14], and the S800 spectrograph [15].

\*Contact author: [sanchez@frib.msu.edu](mailto:sanchez@frib.msu.edu)

†Contact author: [iwasaki@frib.msu.edu](mailto:iwasaki@frib.msu.edu)

‡Present address: Lawrence Livermore National Laboratory, Livermore, California 94550, USA.

The RDM measurements [16] allow for a model-independent determination of  $B(E2)$ , and hence  $M_p(E2)$ , and provide a powerful tool when other methods, such as Coulomb excitation, are not applicable.

The  $(11/2^-) \rightarrow 7/2^-$  transition in  $^{39}\text{Ca}$  is expected to be structurally related to the  $2^+ \rightarrow 0^+$  transition in  $^{38}\text{Ca}$  if we naively assume the  $Z = 20$  shell closure and that the  $(11/2^-)$  and  $7/2^-$  states in  $^{39}\text{Ca}$  can be modeled as an  $f_{7/2}$  neutron coupled to a  $^{38}\text{Ca}$   $2^+$  or  $0^+$  core, respectively. In a similar fashion, the  $11/2^- \rightarrow 7/2^-$  transition in  $^{39}\text{K}$  can be related to the  $2^+ \rightarrow 0^+$  transition in  $^{38}\text{Ar}$  if we assume that the  $11/2^-$  and  $7/2^-$  states in  $^{39}\text{K}$  can be formed by an  $f_{7/2}$  proton coupled to an  $^{38}\text{Ar}$  core. However, the situation is more complicated since there can also be wave function components coming from coupling of a proton ( $^{39}\text{Ca}$ ) or neutron ( $^{39}\text{K}$ ) to states of a  $^{38}\text{K}$  core. Therefore, the present study of the quadrupole transitions in  $^{39}\text{Ca}$  and its mirror  $^{39}\text{K}$  aims to examine the  $B(E2)$  trend as a function of the isospin projection. The data are also compared to shell-model calculations which employ effective interactions available to date in this mass region to understand the role of proton and neutron excitations near  $Z = N = 20$ .

## II. EXPERIMENT

The experiment was performed at the National Superconducting Cyclotron Laboratory. A primary beam of  $^{58}\text{Ni}$  was accelerated at the Coupled Cyclotron Facility up to an energy of 160 MeV/u. The beam impinged upon a  $^9\text{Be}$  production target, producing fragments which were separated by the A1900 fragment separator [11] by means of their magnetic rigidities. The resultant secondary beams of rare isotopes were mainly composed of  $N = 21$  isotones ranging from potassium ( $Z = 19$ ) to vanadium ( $Z = 23$ ) and were identified by their time of flight (TOF) as determined by two plastic scintillators along the beam line. Of the  $N = 21$  isotones, the  $^{42}\text{Sc}$  beam with an energy of 85.2 MeV/u and purity of 44% was selected for the present study as the  $^9\text{Be}(^{42}\text{Sc}, ^{39}\text{Ca})X$  reaction populated excited states of  $^{39}\text{Ca}$  in greater yields than reactions from the other available secondary beams.

The secondary beam was directed to the experimental vault where the lifetime measurements were conducted with the TRiple PLunger for EXotic beams (TRIPLEX) [12]. The excited states of interest were populated by multiple-nucleon removal reactions that occurred in the 2-mm-thick Be target mounted on TRIPLEX. Data were initially taken in the target-only configuration to determine the populations of the excited states. For the purpose of the lifetime measurements with the recoil distance method (RDM) [16], a 0.13-mm-thick Ta degrader was added downstream of the target followed by a 7-mg/cm<sup>2</sup> polyethylene stripper foil to maximize the fraction of fully stripped ions. Data were then taken for two separation distances, 1 and 0 mm, representing the distance settings between the downstream face of the target and the upstream face of the degrader. The recoil nuclei were identified by TOF and energy-loss measurements in the S800 spectrograph [15]; particularly,  $^{39}\text{Ca}$  and  $^{39}\text{K}$  were studied in the present work.

Gamma rays were measured by the Gamma-Ray Energy Tracking In-beam Nuclear Array (GRETINA) [13,14] in

coincidence with outgoing particles identified by the S800 spectrograph [15]. A total of twelve GRETINA detector modules were used for this experiment. The target position of TRIPLEX was located 13 cm upstream with respect to the center of GRETINA. This position was chosen to achieve a good balance between detection efficiency and sensitivity to varying degrees of Doppler shifts caused by different recoil velocities. The segmentation of germanium crystals in GRETINA and the signal decomposition algorithm allow for identification of the gamma-ray interaction point which is used to perform Doppler-shift corrections to the gamma-ray energies [14]. The ion's momentum vector was determined event by event with the S800 spectrograph, allowing us to determine the gamma-ray emission angle with respect to the direction of the recoil nucleus. The gamma-ray emission angle  $\theta$  and ion velocity  $\beta = v/c$  are then used to apply Doppler-shift corrections on an event-by-event basis to produce the in-beam gamma-ray spectra.

## III. DATA ANALYSIS AND RESULTS

### A. $^{39}\text{Ca}$ target-only data

The target-only spectrum measured for  $^{39}\text{Ca}$  is provided in Fig. 1. This figure presents the energy spectrum for gamma rays measured by all GRETINA detectors where Doppler-shift corrections were applied with the gamma-ray emission angle  $\theta$  and ion velocity at the downstream face of the target,  $\beta = 0.33$ . The cascade originating from the  $(15/2^+)$  state at 6432 keV, which subsequently populated the  $(11/2^-)$  state at 3891 keV, was clearly observed in the target-only gamma-ray spectrum. The corresponding partial level scheme is given in Fig. 2 where the relative gamma-ray intensities are indicated by the widths of the arrows. This spectrum was compared to a simulation which utilizes the GEANT4 [18–20] package developed to reproduce RDM experiments utilizing TRIPLEX and GRETINA [20–23]. The gamma-ray transitions indicated by arrows in Fig. 2 were included in the simulation. Background contributions from neutron-induced reactions were evaluated in the laboratory frame and their responses in the ion frame were simulated and included in the fit [21]. Two exponential functions are assumed for the background and the simulation was fit to the data using the log-likelihood method.

Gamma-gamma coincidence was used to verify that the gamma-ray transitions observed in Fig. 1 belong to the cascade shown in Fig. 2, with the 6432-keV  $(15/2^+)$  state being the highest populated. Direct populations to all excited states in the cascade from the  $^9\text{Be}(^{42}\text{Sc}, ^{39}\text{Ca})X$  reactions were determined from the intensities of the gamma-ray peaks in the target-only spectrum, with considerations given to indirect populations from the observed higher-lying states. Each of the population values has been normalized to make their sum 100%. Direct population to the ground state was not calculated, nor were populations to unobserved states, due to the absence of gamma-ray peaks to analyze. Reactions on the target resulted in a weak direct population of 11(3)% to the 6432-keV  $(15/2^+)$  state, which then decays by emission of the 1030-keV gamma ray to the  $(13/2^-)$  state. We observed

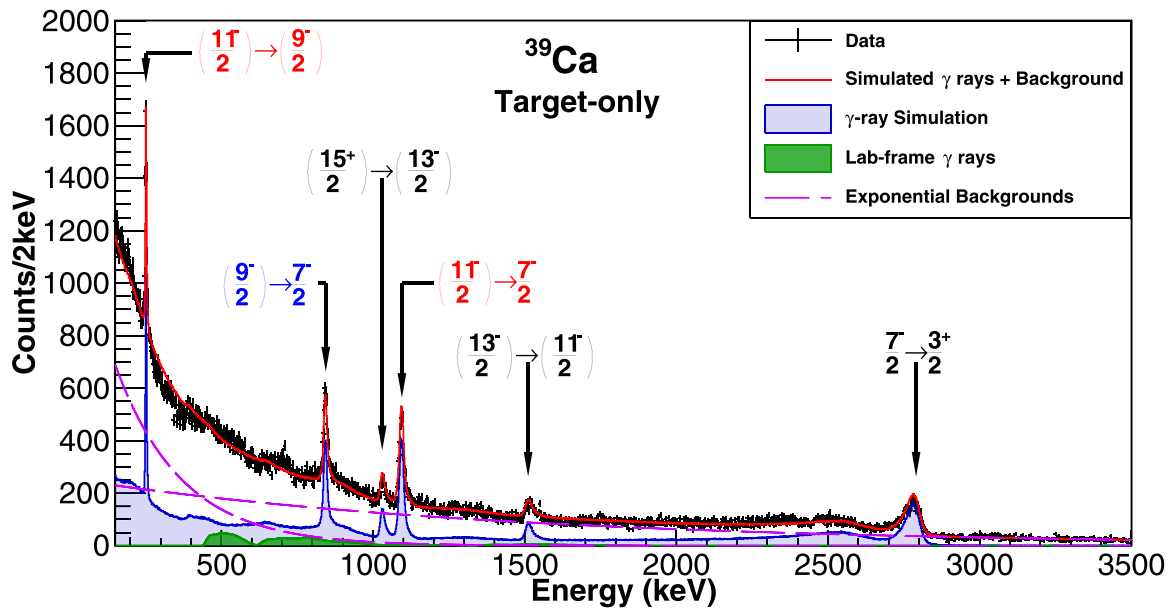


FIG. 1. Doppler-corrected gamma-ray spectrum for  $^{39}\text{Ca}$  from the target-only measurement. Transitions from the  $(11/2^-)$  state are labeled in red, from which the lifetime is determined in the present work. Gamma rays from the  $(9/2^-)$  state are labeled in blue, for which we provide an improved lifetime result.

the weakest direct population of 1(1)% to the 5402-keV  $(13/2^-)$  state, which decays by emission of the 1511-keV gamma ray to the  $(11/2^-)$  state. The largest direct population of 37(8)% was observed for the 3891-keV  $(11/2^-)$  state, which emits the 252-keV gamma ray decaying to the  $(9/2^-)$  state and the 1095-keV gamma ray decaying to the  $7/2^-$  state. A direct population of 17(4)% was determined for the 3640-keV  $(9/2^-)$  state, which decays via the 844-keV gamma-ray transition to the 2796-keV  $7/2^-$  state. Finally we found a direct population of 34(10)% to the  $7/2^-$  state, which decays directly to the  $3/2^+$  ground state. One may also note that we did not observe the population to the  $1/2^+$  state at 2467 keV in our target-only measurement, as was the case for a recent study of  $^{39}\text{Ca}$  by Gade *et al.* [24]. The relative branching ratio of the 252-keV gamma ray  $b_{\text{rel}} = 43(3)$  with respect to the 1095-keV gamma-ray branch  $b_{\text{rel}} = 100(6)$  for the  $(11/2^-)$  state was calculated from the gamma-ray intensities. Within quoted uncertainties, our result agrees with the adopted value of the relative branching ratio for the 252-keV branch,  $b_{\text{rel}} = 51(6)$  [17]. Based on our relative branching ratio, we find an absolute branching ratio  $b_{\text{abs}} = 70(2)\%$  for the 1095-keV decay.

### B. $^{39}\text{Ca}$ RDM analysis

Having determined the populations of excited states from the target-only data, we move to the analysis of the recoil-distance lifetime data. The measured spectrum for the 1-mm target-degrader separation is presented in Fig. 3, where Doppler-shift correction was performed with  $\beta = 0.29$ , corresponding to the velocity of the ions on the downstream face of the degrader. The spectrum measured with the 0-mm separation is presented in Fig. 4 and was corrected for Doppler shifts with the same  $\beta$  value.

Excited states with lifetimes to which the target-degrader configuration is sensitive show a characteristic double-peak structure in the gamma-ray spectrum. These structures can be seen in the 1-mm spectrum for the  $(11/2^-) \rightarrow 7/2^-$  and  $(11/2^-) \rightarrow (9/2^-)$  transitions labeled in red and the  $(9/2^-) \rightarrow 7/2^-$  transition in blue, in Fig. 3. The two components of the gamma-ray double-peak structure are defined by their decay location along the ion trajectory; gamma rays emitted before an ion reaches the degrader are denoted “fast” components while gamma rays emitted after an ion passes through the degrader are called “slow” components.

Since the Doppler-shift correction was optimized for decays behind the degrader, the slow components appear at the proper ion-frame energies for the transitions. On the other hand, the fast components are under-corrected and therefore appear at higher energies. For instance, in Fig. 3, gamma rays from the  $(11/2^-)$  state emitted after the degrader compose the true energy peak at 1095 keV, whereas those emitted before the degrader form the higher-energy fast-component peak observed at 1150 keV, having been undercorrected by the choice of lower  $\beta$ . Based on the mirror states in  $^{39}\text{K}$ , the  $(15/2^+)$  and  $(13/2^-)$  states in  $^{39}\text{Ca}$  are both expected to have lifetimes that are relatively short for this target thickness and foil separation, and, in Fig. 3, we observe only the fast components of the transitions at 1060 and 1570 keV, respectively. The  $7/2^-$  peak at 2796 keV has been omitted from the analysis as it has no effect on the lifetime of the higher lying states. We also note from Fig. 4 that when the target-degrader separation is 0 mm we observe a diminished fast component; this is consistent with more decays occurring behind the degrader.

For recoil-distance lifetime measurements with relativistic-energy beams, it is important to understand and constrain contributions of reactions occurring within the degrader, which can act as a second target to populate excited states of

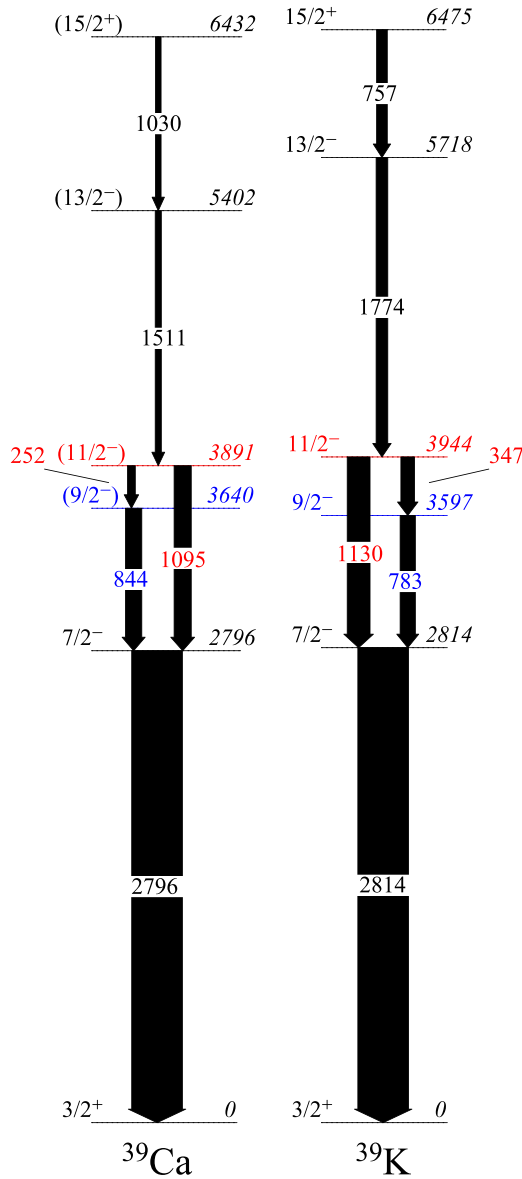


FIG. 2. Level diagrams for gamma rays observed in the target-only spectra for  $^{39}\text{Ca}$  (left) and  $^{39}\text{K}$  (right). The energy information is from Ref. [17] and rounded to keV. The relative intensities of the observed gamma-ray transitions, indicated by the widths of the arrows, are normalized to the intensity of the  $7/2^- \rightarrow 3/2^+_{\text{g.s.}}$  transition for the respective nuclei. The energy information for the  $11/2^-$  state is highlighted in red, while those for the  $9/2^-$  state are highlighted in blue.

interest. In practice, the ratio of reactions on target to reactions on degrader should be quantified to obtain the best possible parameter set in our simulations [25]. To quantify this ratio we used the 1-mm separation data and analyzed the transitions from the  $(15/2^+)$  and  $(13/2^-)$  states, which are expected to be short-lived with respect to flight time over the foil separation. As can be observed in Fig. 3, both transitions from the  $(15/2^+)$  and  $(13/2^-)$  states are dominated by their fast components, with very little hint of slow components for each transition. Since the lifetimes of these states are not known [17], we

estimated their lifetimes from the available data for analogue states in  $^{39}\text{K}$  after taking into account the energy differences of the decays based on the  $1/E_\gamma^{2L+1}$  dependence. We assumed a dipole ( $L = 1$ ) transition for the  $(15/2^+) \rightarrow (13/2^-)$  case as the quadrupole component with  $\delta(M2/E1) = 0.002$  [17] is negligible, and we calculated a mean lifetime of  $\tau = 4.8$  ps for the  $(15/2^+)$  state of  $^{39}\text{Ca}$ . For the  $(13/2^-) \rightarrow (11/2^-)$  transition in  $^{39}\text{Ca}$  we also assumed a prominent dipole component as the evaluation of the  $(13/2^-)$  state yields a 6% quadrupole component (from  $\delta(E2/M1) = -0.25$  [17]) based on data for analogue states in  $^{39}\text{K}$ , from which we estimated a lifetime of  $\tau = 0.4$  ps. Therefore, both states in  $^{39}\text{Ca}$  are expected to be relatively short-lived compared to our 1-mm separation distance and the relatively thick (2 mm) target which effectively increases the foil separation. The gamma-ray spectra including the  $(15/2^+) \rightarrow (13/2^-)$  and  $(13/2^-) \rightarrow (11/2^-)$  transitions were then simulated as a cascade to account for feeding effects on the  $(13/2^-)$  state. By adjusting the ratio of reactions on target to degrader within our simulation, we determined a lower limit of the ratio to be 15(1) : 1, indicating that reactions on the target are dominant compared to those on the degrader in the  $^{39}\text{Ca}$  data. Therefore, the lifetime results remain consistent within statistical errors even if we alter this ratio in the range of 13–17 in the analysis.

Using the direct populations and the target-degrader reaction ratio calculated above, simulations for the cascade in Fig. 2 were performed with a wide range of lifetimes for the states of interest. The lifetime range was then narrowed down accordingly with fit results. The analysis of the  $(11/2^-)$  state was conducted utilizing both the 1095- and 252-keV branches, leading to the lifetime result of  $\tau_{11/2^-} = 37(1)$  ps for the 1095-keV branch and  $\tau_{11/2^-} = 37^{(+1)}_{(-2)}$  ps for the 252-keV branch, where the error is statistical only.

To evaluate additional systematic errors, the direct population of the  $(15/2^+)$  state was varied and the effect on the lifetime of the  $(11/2^-)$  state was examined. Since the direct population of the  $(13/2^-)$  state was consistent with zero within uncertainty, it was determined that variation of the  $(15/2^+)$  direct population was the dominant contributor to systematic uncertainties. Due to feeding effects from the population of the  $(15/2^+)$  and  $(13/2^-)$  states, we determined a  $^{(+1)}_{(-4)}_{\text{sys}}$  ps systematic uncertainty for the mean lifetime of the  $(11/2^-)$  state. Similarly, the lifetime of the  $(15/2^+)$  state was varied within our simulations and its effects on the lifetime of the  $(11/2^-)$  state were evaluated. From feeding effects due to the lifetimes of the  $(15/2^+)$  and  $(13/2^-)$  states we found an additional systematic uncertainty of  $^{(+1)}_{(-3)}_{\text{sys}}$  ps for our result.

The systematic uncertainties were added in quadrature with the statistical uncertainties and are presented below as a single, combined error to our lifetime results. The analysis of the 1095-keV branch resulted in a lifetime of  $\tau_{11/2^-} = 37^{(+2)}_{(-5)}$  ps. The analysis of the 252-keV branch yields the same result as the 1095-keV branch with a lifetime of  $\tau_{11/2^-} = 37^{(+2)}_{(-5)}$  ps. The agreement of the lifetimes from the evaluation of both the 252- and 1095-keV branches strengthened confidence in the analysis. For the purpose of this study we adopt a mean lifetime  $\tau_{11/2^-} = 37^{(+2)}_{(-5)}$  ps for the  $(11/2^-)$

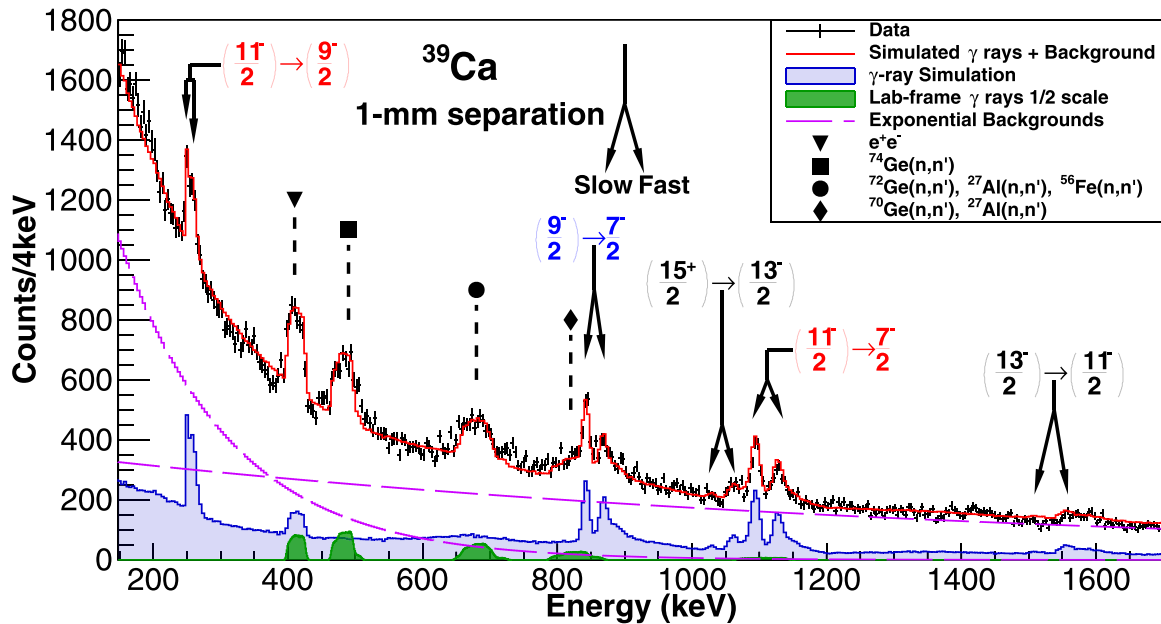


FIG. 3. Doppler-corrected gamma-ray spectrum for  $^{39}\text{Ca}$  taken with the 1-mm target-degrader separation. The spectrum has been gated for the gamma-ray emission angle between  $\theta = 29^\circ$  and  $\theta = 46^\circ$  to improve sensitivity to Doppler shifts. Transitions from the  $(11/2^-)$  state are labeled in red, while transitions from the  $(9/2^-)$  state are labeled in blue. Laboratory-frame background gamma rays, associated with neutron-induced reactions [21], are shown in green and downscaled by a factor of 2 for clarity. As a result of the angle gate, the laboratory-frame background contributions present peak-like structures which are not observed in the ungated target-only spectrum shown in Fig. 1.

state in  $^{39}\text{Ca}$ . Using the lifetime above, the absolute branching ratio of the  $(11/2^-) \rightarrow 7/2^-$  transition  $b_{\text{abs}} = 70(2)\%$ , and the gamma-ray energy  $E_\gamma = 1095(4)$  keV, we determined the reduced transition strength  $B(E2; (11/2^-) \rightarrow 7/2^-) = 9.8^{(+14)}_{(-6)} e^2\text{fm}^4$  as summarized in Table I.

A measurement of the lifetime of the  $(9/2^-)$  state in  $^{39}\text{Ca}$  was also obtained in the present study. Due to the large population of the  $(11/2^-)$  state and its long lifetime when compared to the  $(15/2^+)$  state, the feeding effect from the  $(11/2^-)$  state is the dominant source of the uncertainty in the

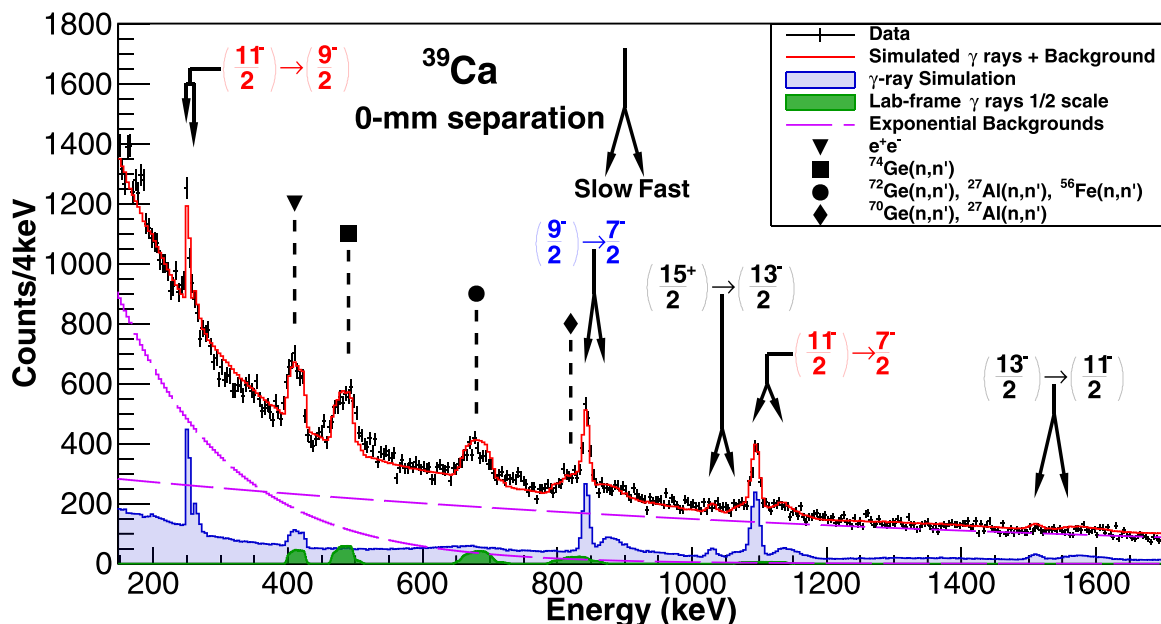


FIG. 4. Doppler-shift corrected gamma-ray spectrum for  $^{39}\text{Ca}$  taken with the 0-mm target-degrader separation setting. The spectrum has been gated between  $\theta = 29^\circ$  and  $\theta = 46^\circ$  to improve sensitivity to Doppler shifts. Transitions from the  $(11/2^-)$  state are labeled in red, while transitions from the  $(9/2^-)$  state are labeled in blue. Laboratory-frame background gamma rays are shown in green and downscaled by a factor of 2.

TABLE I. The present results (Exp) of  $B(E2)$ , proton ( $M_p$ ) and neutron ( $M_n$ ) matrix elements for the  $11/2^- \rightarrow 7/2^-$  transitions of  $^{39}\text{Ca}$  and  $^{39}\text{K}$  are compared to shell-model calculations with the FSU [27], ZBM2 [28], and ZBM2m [29] effective interactions. The  $M_n$  values and  $M_n/M_p$  ratios are presented only for  $^{39}\text{Ca}$  and corresponding values in mirror  $^{39}\text{K}$  are omitted to avoid redundancy.

		$B(E2)$ ( $e^2\text{fm}^4$ )	$M_p$ ( $e\text{fm}^2$ )	$M_n$ ( $e\text{fm}^2$ )	$M_n/M_p$
$^{39}\text{Ca}$	Exp	$9.8^{(+14)}_{(-6)}$	$10.8^{(+8)}_{(-4)}$	16.4(13)	1.5(2)
	FSU	3.4	6.4	11.4	1.8
	ZBM2	20.6	15.7	18.0	1.1
	ZBM2m	13.7	12.8	14.9	1.2
$^{39}\text{K}$	Exp	22.4(35)	16.4(13)		
	FSU	10.8	11.4		
	ZBM2	27.0	18.0		
	ZBM2m	18.5	14.9		

lifetime measurement of the  $(9/2^-)$  state. We first determined a value of  $\tau_{9/2^-} = 22(1)$  ps, where the error is statistical only. Following the procedure described above, the population of the  $(11/2^-)$  state was altered and its effect on the lifetime of the  $(9/2^-)$  state was evaluated. We determined that the population of the  $(11/2^-)$  state contributes a  $(^{+4}_{-6})_{\text{sys}}$  ps systematic uncertainty to our measurement of the lifetime of the  $(9/2^-)$  state. The lifetime of the  $(11/2^-)$  state was then altered within the uncertainties determined above and the effect on the lifetime of the  $(9/2^-)$  state was evaluated. Due to the uncertainty in the lifetime of the  $(11/2^-)$  state, an additional systematic uncertainty of  $(\pm 4)_{\text{sys}}$  ps was found for our lifetime measurement of the  $(9/2^-)$  state. The systematic uncertainties were added in quadrature with the statistical uncertainty, resulting

in the lifetime of  $\tau_{9/2^-} = 22(^{+6}_{-7})$  ps. This lifetime agrees with the adopted value of  $\tau = 24(15)$  ps measured by Kessel *et al.* [26] while providing improved precision.

### C. $^{39}\text{K}$ target-only data

The analysis method used for  $^{39}\text{Ca}$  was tested and validated by studying the reference data for the mirror nucleus  $^{39}\text{K}$ , for which the  $^9\text{Be}(^{42}\text{Sc}, ^{39}\text{K})X$  reaction was employed. The gamma-ray spectrum for the target-only data is presented in Fig. 5 with the analogue cascade of transitions originating from the  $15/2^+$  state noted with arrows, as observed in  $^{39}\text{Ca}$ . The relevant level scheme of  $^{39}\text{K}$  is provided in Fig. 2 and the analogue transitions in  $^{39}\text{K}$  that are the focus of this work are highlighted in red and blue.

In Fig. 5 one may notice transition peaks near 900 and 1400 keV which are not labeled; we have chosen to omit these transitions from our analysis because the associated states do not significantly populate the  $11/2^-$  state, as explained below. The  $7/2_4^-$  state at 5010 keV was populated in our experiment and decays via two branches; the prominent branch emits a 883-keV gamma ray to the  $7/2_2^-$  state at 4127 keV which, in turn, decays by cascade to the  $7/2_1^-$  state at 2814 keV via emission of a 1312-keV gamma ray. The minor branch of the  $7/2_4^-$  state decays by emission of a 1412-keV gamma ray to the  $9/2_1^-$  state at 3597 keV with an absolute branching ratio of  $b_{\text{abs}} = 23(4)\%$ . Therefore, decays from the  $7/2_4^-$  state bypass the  $11/2_1^-$  state of interest and have no effect on the lifetime measurement of the  $11/2_1^-$  state. We also observed transitions from the  $9/2_2^-$  state at 4520 keV whose largest branch leads to the  $9/2_1^-$  state at 3597 keV by emission of a 923-keV gamma ray. The  $9/2_2^-$  state also has a minor branch which feeds the  $11/2_1^-$  state at 3944 keV by emission of a 576-keV gamma ray which we do not observe in our data. The absolute

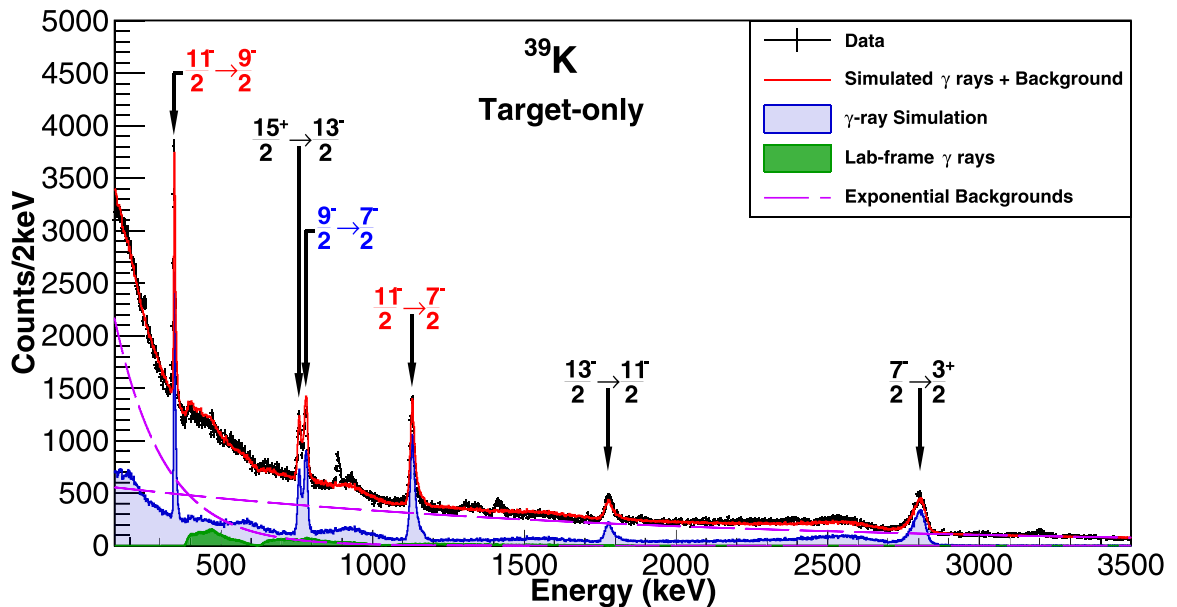


FIG. 5. Doppler-shift corrected gamma-ray spectrum for  $^{39}\text{K}$  from the target-only measurement. Transitions from the  $(11/2^-)$  state are labeled in red, while transitions from the  $(9/2^-)$  state are labeled in blue. The peak structures at 900 and 1400 keV, which are not labeled in the spectrum, are ascribed to transitions which do not strongly populate the  $11/2^-$  state of interest (see text for details).

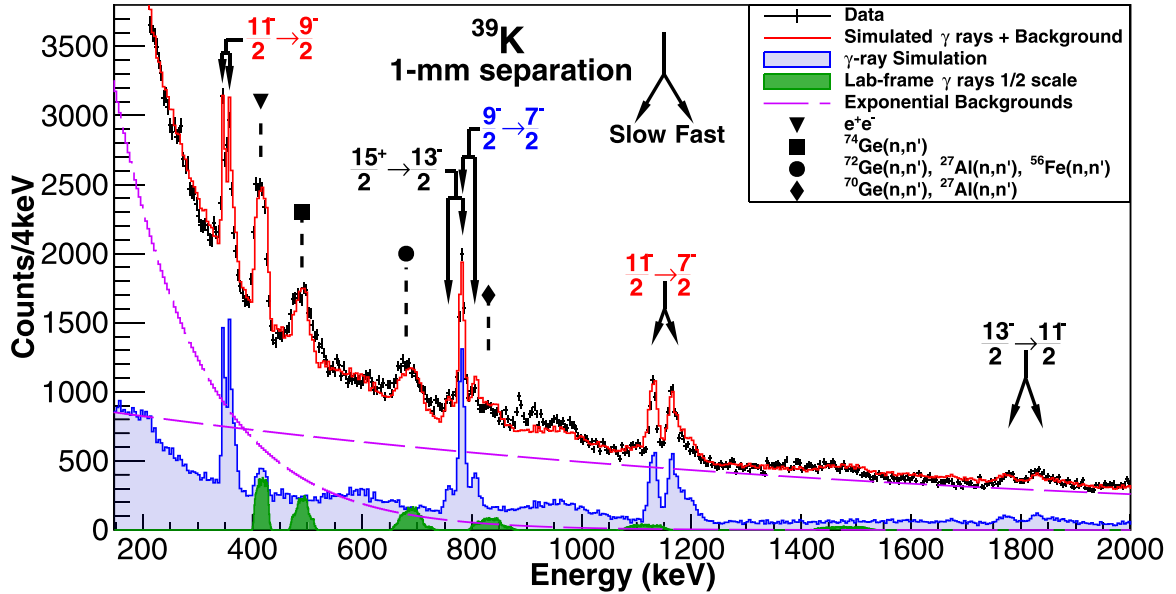


FIG. 6. Doppler-shift corrected gamma-ray spectrum for the 1-mm target-degrader separation setting in  $^{39}\text{K}$ . The spectrum has been gated between  $\theta = 29^\circ$  and  $\theta = 46^\circ$  to improve sensitivity to Doppler shifts. Transitions from the  $(11/2^-)$  state are labeled in red, while transitions from the  $(9/2^-)$  state are labeled in blue. Laboratory-frame background gamma rays are shown in green and downscaled by a factor of 2.

branching ratio for this  $9/2_2^- \rightarrow 11/2_1^-$  transition is weak ( $b_{\text{abs}} = 9.2(8)\%$  [17]) and the state has a short lifetime of  $\tau_{9/2_2^-} = 0.14(4)$  ps [17], from which we conclude that feeding effects to the  $11/2_1^-$  state from the  $9/2_2^-$  state are negligible if any. Thus, we acknowledge the existence of these transitions in our data while determining that their influence on our state of interest is negligible and can therefore be excluded from the analysis, allowing us to focus on the mirror cascade in  $^{39}\text{K}$  as shown in Fig. 2.

When comparing the  $^{39}\text{Ca}$  and  $^{39}\text{K}$  target-only spectra, the similarity of decay schemes is apparent, but one should note a 300-keV increase in the energy of the  $13/2^-$  state in  $^{39}\text{K}$ . This shift displaces the  $15/2^+ \rightarrow 13/2^-$  transition from 1030 keV in  $^{39}\text{Ca}$  to an energy of 757 keV in  $^{39}\text{K}$ , placing it in close proximity to the 783-keV peak from the  $9/2^- \rightarrow 7/2^-$  transition. As with our observations of the fast components of the higher-lying transitions in  $^{39}\text{Ca}$ , the lifetime of the  $13/2^-$  state in  $^{39}\text{K}$  is short ( $\tau_{13/2^-} = 0.27(7)$  ps [17]) and the direct population is small [2(2)%], and therefore the  $13/2^-$  state has a negligible feeding effect on the  $11/2^-$  state.

From the target-only data, a relative branching ratio for the  $11/2^-$  state of  $b_{\text{rel}} = 52(4)$  was determined by the intensity of the 347-keV peak with respect to the intensity of the major branch at 1130 keV ( $b_{\text{rel}} = 100(4)$ ). This result was found to agree with the literature value of the relative branching ratio  $b_{\text{rel}} = 57.3(13)$  [17]. The analysis of the target-only data for  $^{39}\text{K}$  was accomplished by determining the direct population fractions of the populated states via the method explained for  $^{39}\text{Ca}$ . To the  $15/2^+$  state at 6475 keV, we assigned a population of 21(3)%. This state decays via emission of a 757-keV gamma ray to the  $13/2^-$  state. The  $13/2^-$  state at 5718 keV has a direct population of 2(2)% and decays to the  $11/2^-$  state via emission of a 1774-keV gamma ray. Again, we observed the largest population to the  $11/2^-$  state at 3944 keV, for

which we calculated a direct population of 49(7)%. This state decays by emission of either a 347-keV gamma ray to the  $9/2^-$  state or an 1130-keV gamma ray to the  $7/2^-$  state. The  $9/2^-$  state at 3597 keV was observed to be much more weakly populated in the  $^9\text{Be}(^{42}\text{Sc}, ^{39}\text{K})X$  reaction with a direct population of 3(2)%, decaying by emission of a 783-keV gamma ray to the  $7/2^-$  state. Finally, to the 2814-keV  $7/2^-$  state, we find a direct population of 26(10)% with ambiguities due to feeding from states not included in this study.

#### D. $^{39}\text{K}$ RDM analysis

The spectra for  $^{39}\text{K}$  taken with the 1- and 0-mm separation distance are provided in Figs. 6 and 7, respectively. The decrease in the target-degrader ratio, compared to the case of  $^{39}\text{Ca}$ , is evident in the  $13/2^- \rightarrow 11/2^-$  transition measured with the 1-mm distance as shown in Fig. 6, where one can observe comparable yields for the fast and slow components. The effective lifetime of the short-lived  $13/2^-$  state in  $^{39}\text{K}$ , including the feeding from the  $15/2^+$  state ( $\tau_{15/2^+} = 12.1(6)$  ps [17]), was used to determine the ratio of reactions on target to reactions on degrader, which was found to be 2.3(4) : 1. By considering the rigidity setting of the S800 spectrograph, the reduced ratio was attributed to an effect of the momentum acceptance setting, which was sufficient to accept nearly all of the  $^{39}\text{Ca}$  recoil nuclei, but was only able to cover the lower-momentum components of  $^{39}\text{K}$ . Since multinucleon ( $-2p - 1n$ ) removal reactions of  $^{42}\text{Sc}$  are used to populate  $^{39}\text{K}$ , the final momentum of  $^{39}\text{K}$  depends largely on the reaction points, yielding low-momentum components when reactions occur in the degrader. The rigidity setting used in this experiment therefore resulted in the decreased target-degrader ratio. These features are incorporated in the simulation and the target-degrader ratio should be considered as an effective parameter used for the lifetime analysis.

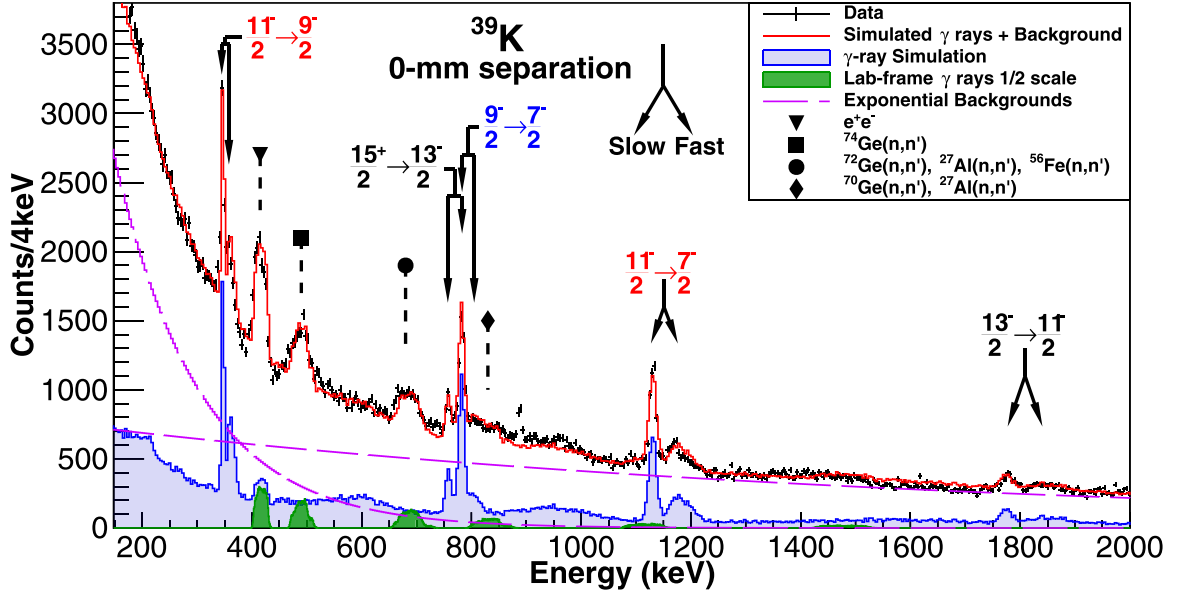


FIG. 7. Doppler-corrected gamma-ray spectrum for the  $^{39}\text{K}$  0-mm target-degrader separation. The spectrum has been gated between  $\theta = 29^\circ$  and  $\theta = 46^\circ$  to improve sensitivity to Doppler shifts. Transitions from the  $(11/2^-)$  state are labeled in red, while transitions from the  $(9/2^-)$  state are labeled in blue. Laboratory-frame background gamma rays are shown in green and downscaled by a factor of 2.

Lifetime analyses of the  $^{39}\text{K}$  states were performed using the adopted lifetime values for higher-lying states [17] combined with the direct population of the excited states determined from the target-only data. By varying the target-degrader ratio and observing the effect on the lifetime of the  $11/2^-$  state we determined that a systematic error of  $(\pm 2)_{\text{sys}}$  ps contributes to the overall uncertainty of the lifetime measurement of the  $11/2^-$  state. As a result, a lifetime of  $\tau_{11/2^-} = 13(2)$  ps was determined for the  $11/2^-$  state at 3944 keV from fits to the 1130- and 347-keV peaks in both the 0- and 1-mm spectra. The statistical and systematic uncertainties were added in quadrature for the result above and our result agrees with the adopted value of 12.3(14) ps. The experimental values for the absolute branching ratio of the 1130(4)-keV branch found from the target-only data  $b_{\text{abs}} = 66(2)\%$  and the lifetime above give the reduced transition strength of  $B(E2; 11/2^- \rightarrow 7/2^-) = 22.4(35) e^2\text{fm}^4$  as presented in Table I.

#### IV. DISCUSSION

The experimental mean lifetimes  $\tau$ , the absolute branching ratios  $b_{\text{abs}}$  for the  $11/2^-$  states, and the gamma-ray energies  $E_\gamma$  given in the previous sections were used to calculate the  $B(E2; 11/2^- \rightarrow 7/2^-)$  values for  $^{39}\text{Ca}$  and  $^{39}\text{K}$  as presented in Table I. The  $B(E2)$  values were then converted to the absolute value of proton matrix elements  $M_p$ ,

$$M_p = \sqrt{B(E2; J_i \rightarrow J_f) \times (2J_i + 1)} \quad (1)$$

with  $J_i = 11/2$ , and are also presented for both nuclei in Table I. Here we note that, under the assumption of isospin conservation, the neutron matrix elements  $M_n$  of  $^{39}\text{Ca}$  can be obtained from the mirror nucleus  $^{39}\text{K}$  via the relation  $M_n(-T_z) = M_p(+T_z)$ , or in our case  $M_n(^{39}\text{Ca}) = M_p(^{39}\text{K})$ ; for more information on this relationship see Ref. [3]. One

should note that the  $M_p(T_z)$  values for our  $A = 39$  mirror nuclei increase with the increasing  $T_z$ , which results in  $M_n > M_p$  for  $^{39}\text{Ca}$ . This implies that the  $A = 39$  mirror nuclei have a negative isovector matrix element  $M_1$  [3,23]. The trend observed in the  $A = 39$  and previously studied  $A = 38$  [4,5] systems is opposite to the  $T_z$  dependence in many isospin multiplets, as shown in Fig. 2 of Ref. [5]. The ratios  $M_n/M_p$  observed among neutron-deficient calcium isotopes are found to be 0.8 and 1.1 for the  $2^+ \rightarrow 0^+$  transitions of  $^{36}\text{Ca}$  and  $^{38}\text{Ca}$  [9], respectively, and 1.5 for the  $11/2^- \rightarrow 7/2^-$  transition of  $^{39}\text{Ca}$ , indicating an increased degree of neutron excitations toward  $N = Z$ .

The experimental  $B(E2)$  values of  $^{39}\text{Ca}$  as well as the proton matrix elements  $M_p$  and neutron matrix elements  $M_n$  are compared to shell-model calculations with three effective interactions commonly used in this mass region: FSU [27], ZBM2 [28], and ZBM2m [29]. The proton matrix element  $M_p$  is calculated from the bare proton and neutron matrix elements  $A_p$  and  $A_n$  via the following formula by incorporating the effective charges  $e_p$  and  $e_n$ :

$$M_p = e_p A_p + e_n A_n. \quad (2)$$

By assuming isospin symmetry [3], the neutron matrix element  $M_n$  can be obtained from:

$$M_n = e_p A_n + e_n A_p. \quad (3)$$

The calculated values of  $A_p$  and  $A_n$  are summarized in Table II. For each calculation, we used the empirical effective charges of  $e_p(sd) = 1.36$  and  $e_n(sd) = 0.45$ , which are based on a comparison of a large set of  $E2$  observables within the  $sd$  model space with the USDB Hamiltonian [30]. In Ref. [9], these  $sd$ -effective charges were used with the ZBM2 model space for the  $B(E2)$  values of  $^{36,38}\text{Ca}$ ,  $^{36}\text{S}$ , and  $^{38}\text{Ar}$ . Effective charges can also be derived from calculations of core-polarization ( $cp$ ) effects such as those given in Ref. [31]



TABLE II. The calculated values of the bare proton ( $A_p$ ) and neutron ( $A_n$ ) matrix elements for the  $11/2^- \rightarrow 7/2^-$  transition of  $^{39}\text{Ca}$  (top) and  $2^+ \rightarrow 0^+$  transition of  $^{38}\text{Ca}$  (bottom) from shell-model calculations with the FSU [27], ZBM2 [28], and ZBM2m [29] effective interactions.

		$A_p$ ( $e\text{fm}^2$ )	$A_n$ ( $e\text{fm}^2$ )
$^{39}\text{Ca}$ ( $11/2^- \rightarrow 7/2^-$ )	FSU	2.14	7.65
	ZBM2	8.06	10.57
	ZBM2m	6.51	8.81
$^{38}\text{Ca}$ ( $2^+ \rightarrow 0^+$ )	FSU	0.00	8.31
	ZBM2	5.00	8.19
	ZBM2m	5.10	8.16

where values of  $e_p(cp) = 1.31$  and  $e_n(cp) = 0.46$  were obtained. These  $cp$ -effective charges are comparable with the above  $sd$ -effective charges and were used in the  $sd$ - $pf$  model space with the SDPF-U-MIX Hamiltonian for calculations of  $^{36}\text{Ca}$  and  $^{36}\text{S}$  [32]. Similar effective charges were also used to reproduce  $E2$  data for neutron-rich magnesium isotopes [33]. As in Ref. [28] for the ZBM2 model space, one sometimes uses the standard (default, denoted as  $d$ ) effective charges of  $e_p(d) = 1.5$  and  $e_n(d) = 0.5$ . These default values work well in the  $fp$  model space for  $E2$  data in the region of  $A = 47$ – $72$  [34].

As shown in Ref. [9], the  $E2$  observables in this region are very sensitive to the amount of  $sd$ - $pf$  mixing. For this reason, it is not possible to determine effective charges for the ZBM2 model space by comparison of experimental and calculated  $E2$  data. Rather, one has to start with a reasonable set of effective charges, and then attribute deviations between experiment and theory in terms of deficiencies in the wave functions as well as the effective charges. For consistency with calculations for  $^{38}\text{Ca}$  and  $^{38}\text{Ar}$  given in Ref. [9], we used the  $sd$ -effective charges. Overall, in comparison with  $E2$  data, the isoscalar-effective charge  $e_p + e_n$  is the most important combination, with  $e_p(sd) + e_n(sd) = 1.81$ ,  $e_p(cp) + e_n(cp) = 1.77$ , and  $e_p(d) + e_n(d) = 2.0$ . If the ZBM2 wave functions for  $^{38}\text{Ca}$  and  $^{38}\text{Ar}$  were correct, one would need  $e_p + e_n = 1.61(4)$  based on data for the  $A = 38$  system. This value is closer to the values from the  $sd$ - and  $cp$ -effective charges, while the relatively small value may point to deficiencies in the ZBM2 wave functions.

To begin our discussion on  $^{39}\text{Ca}$ , we compare our results with the FSU calculation as presented in Table I. Based on pure  $n$ -particle– $n$ -hole configurations up to  $0\hbar\omega$ ,  $1\hbar\omega$ , and  $2\hbar\omega$  excitations in the  $spsdpf$  model space, the FSU interaction provides accurate predictions of level energies for nuclei in the  $sd$ -shell region, including neutron-rich nuclei in the island of inversion [27]. For the presently studied negative-parity states, we consider the  $1\hbar\omega$  configurations, and the calculated level energies are compared to data in Fig. 8. In the case of  $^{39}\text{Ca}$ , the FSU calculations are in good agreement with the experimental level scheme. For the  $11/2^-$  state with a pure  $1\hbar\omega$  configuration, the FSU interaction predicts approximately 60% proton excitations and 40% neutron excitations into the  $fp$  shell. Interestingly, the calculated  $1\hbar\omega$  configuration is due to both proton and neutron contributions.

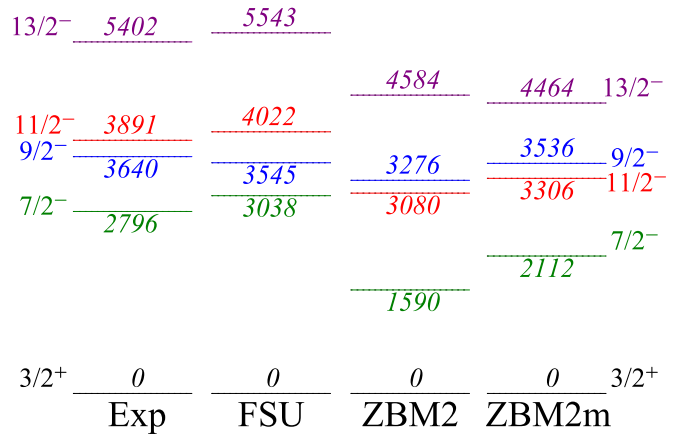


FIG. 8. Level energies of the lowest  $7/2^-$ ,  $9/2^-$ ,  $11/2^-$ , and  $13/2^-$  states of  $^{39}\text{Ca}$  from experiment (Exp) compared to shell-model calculations with the FSU [27], ZBM2 [28], and ZBM2m [29] effective interactions.

The  $M_n/M_p$  ratio of 1.8 is slightly overestimated compared to the experimental value. The absolute values of  $B(E2)$  and each matrix element in the FSU calculations are smaller than the data, suggesting possible roles of higher-order cross-shell excitations.

The ZBM2 calculations were performed in a smaller model space of the  $2s_{1/2}$ ,  $1d_{3/2}$ ,  $1f_{7/2}$ , and  $2p_{3/2}$  orbitals while allowing all configurations within this space [28]. The ZBM2 interaction was developed to reproduce the odd-even charge radii staggering in the  $^{40}\text{Ca}$  to  $^{48}\text{Ca}$  isotopic chain while simultaneously replicating the parabolic dependence on mass  $A$  of the low-lying excited-state energies [28]. The composition of the  $11/2^-$  state of  $^{39}\text{Ca}$  is summarized in Table III (top) giving configurations in terms of  $\Delta_p$  and  $\Delta_n$ , where  $\Delta_p$  ( $\Delta_n$ ) is the number of protons (neutrons) excited from the  $(2s_{1/2}, 1d_{3/2})$  to  $(1f_{7/2}, 2p_{3/2})$  orbitals. The lowest-order excitations with  $(\Delta_p, \Delta_n)$  values of  $(1,0)$  and  $(0,1)$  are 26% and 21% respectively, which are followed by higher-order

TABLE III. The numbers of protons ( $\Delta_p$ ) and neutrons ( $\Delta_n$ ) excited from the  $(2s_{1/2}, 1d_{3/2})$  to  $(1f_{7/2}, 2p_{3/2})$  orbitals calculated with the ZBM2 [28] and ZBM2m [29] interactions. The percentages (%) for different configurations are given for the  $11/2^-$  state of  $^{39}\text{Ca}$  (top) and for the  $2^+$  state of  $^{38}\text{Ca}$  (bottom). The percentage for each of the higher-order configurations is less than 6%, and only the sum of these configurations is listed as “other” in the table.

	$\Delta_p$	$\Delta_n$	ZBM2 (%)	ZBM2m (%)
$^{39}\text{Ca}$ ( $11/2^-$ )	1	0	26	38
	0	1	21	18
	2	1	23	20
	1	2	10	9
		other	20	15
$^{38}\text{Ca}$ ( $2^+$ )	0	0	36	39
	2	0	30	32
	1	1	11	10
		other	23	19

excitations of  $(\Delta_p, \Delta_n) = (2, 1)$  with 23% and  $(1, 2)$  with 10%. Both protons and neutrons contribute to the cross-shell excitations, providing an enhancement of  $M_p$  accompanied by an enhanced  $M_n$  value for  $^{39}\text{Ca}$ . By examining the bare  $A_p$  and  $A_n$  values shown in Table II (top), both values are larger than those calculated by the FSU interaction. As for the comparison to the data, the ZBM2 interaction overestimates  $M_p$  and  $B(E2)$  with a reduced  $M_n/M_p$  ratio. In addition, the ZBM2 calculation predicts the energy for the  $11/2^-$  state approximately 800 keV lower than the experimental value, resulting in the inversion of the  $9/2^-$  and  $11/2^-$  states as shown in Fig. 8.

In order to present a comparison with alternative theoretical calculations, we also employed the modified version of the ZBM2 interaction [29], denoted as ZBM2m. This interaction was developed in Ref. [29] to better describe the charge radius of the  $^{38}\text{K}^m$  isomer and reproduce the correct order of the  $3^+$  ground state and  $0^+$  isomeric state of  $^{38}\text{K}$ . As with the ZBM2 interaction, the ZBM2m interaction utilizes the above-mentioned *sdfp* model space. We observe in Table I that the ZBM2m predictions most closely agree with the experimental  $B(E2)$ ,  $M_p$ , and  $M_n$  values of  $^{39}\text{Ca}$ . As shown in Table III, the  $(11/2^-)$  state has a larger  $(\Delta_p, \Delta_n) = (1, 0)$  component compared to the original ZBM2 calculations. While the ZBM2m results of  $M_p$  and  $M_n$  are reduced compared to the ZBM2 calculations, the enhancement over the FSU results is still significant. Indeed, compared to the FSU calculations, the enhanced values of  $A_p$  and  $A_n$  are evident in Table II (top). A further increase of  $A_n$  may be favored given that the ZBM2m interaction underestimates the  $M_n/M_p$  ratio. In Fig. 8, the excitation energy of the  $11/2^-$  state predicted by the ZBM2m interaction is 600 keV lower than the data, showing slight improvement over the ZBM2 result. Based on the ZBM2m (ZBM2) wave functions and present data, the isoscalar-effective charge,  $e_p + e_n$ , would correspond to the value of 1.78(10) [1.46(8)] for the  $A = 39$  system. The present experimental data supports the ZBM2m calculations for both  $M_p$  and  $M_n$  of  $^{39}\text{Ca}$ , which emphasizes the important role of cross-shell excitations of both protons and neutrons across the  $Z = N = 20$  shell gap.

Finally, to understand the isospin decomposition of the  $E2$  strengths in the  $A = 38$  triplet, we also compared the present shell-model calculations to available data [9,17] of the  $B(E2)$  and  $M_p$  values for the  $2^+ \rightarrow 0^+$  transitions in  $^{38}\text{Ca}$ ,  $^{38}\text{K}$ , and  $^{38}\text{Ar}$  as summarized in Table IV. The  $M_n$  value of  $^{38}\text{Ca}$  was obtained from the  $M_p$  value of the mirror  $^{38}\text{Ar}$  [3]. The same set of interactions and effective charges as employed for  $^{39}\text{Ca}$  were used. The calculated values of the bare  $E2$  matrix elements  $A_p$  and  $A_n$  are also shown in Table II (bottom). We first note that, following recent evaluations which suggest additional systematic errors for  $^{38}\text{K}$  data [35], the linear trend of  $M_p$  values is not completely ruled out among the  $A = 38$  system. However, the enhanced collectivity in  $^{38}\text{Ca}$  is still evident, as the  $M_n/M_p$  ratio of 1.1(1) indicates sizable proton excitations. With the presently used effective charges, the enhanced  $B(E2)$  and  $M_p$  values in  $^{38}\text{Ca}$  are well reproduced by the ZBM2 and ZBM2m calculations, although it appears that these calculations overestimate the  $M_n$  value of  $^{38}\text{Ca}$  as well as  $M_p$  values of  $^{38}\text{K}$  and  $^{38}\text{Ar}$ . The two calculations

TABLE IV. The experimental data (Exp) of  $B(E2)$ , proton ( $M_p$ ) and neutron ( $M_n$ ) matrix elements for the  $2^+ \rightarrow 0^+$  transitions of the  $T = 1$  triplet  $^{38}\text{Ca}$ ,  $^{38}\text{K}$ , and  $^{38}\text{Ar}$  are compared to shell-model calculations with the FSU [27], ZBM2 [28], and ZBM2m [29] effective interactions. The  $M_n$  values and  $M_n/M_p$  ratios are presented only for  $^{38}\text{Ca}$ .

		$B(E2)$ ( $e^2\text{fm}^4$ )	$M_p$ ( $e\text{fm}^2$ )	$M_n$ ( $e\text{fm}^2$ )	$M_n/M_p$
$^{38}\text{Ca}$	Exp	20.2(22)	10.0(5)	11.3(2)	1.1(1)
	FSU	2.8	3.7	11.3	3.0
	ZBM2	22.0	10.5	13.4	1.3
$^{38}\text{K}$	ZBM2m	22.5	10.6	13.4	1.3
	Exp	13( $^{+10}_6$ )	8( $^{+3}_2$ )		
	FSU	11.3	7.5		
$^{38}\text{Ar}$	ZBM2	28.5	11.9		
	ZBM2m	28.8	12.0		
	Exp	25.6(8)	11.3(2)		
	FSU	25.5	11.3		
	ZBM2	35.8	13.4		
	ZBM2m	35.9	13.4		

yield similar wave-function components for the  $2^+$  state in  $^{38}\text{Ca}$ , as shown in Table III, showing nearly identical  $B(E2)$  results. This is in contrast to the  $A = 39$  case, where  $B(E2)$  values are more sensitive to the modification of the ZBM2 interaction because negative parity states, such as the  $11/2^-$  state in  $^{39}\text{Ca}$ , contain more one-particle–one-hole excitations which are directly influenced by the size of the  $Z = N = 20$  gap. As shown in Fig. 8, the ZBM2m calculations present a larger level spacing between the lowest  $7/2^-$  and  $3/2^+$  states indicative of an increased gap, which resulted in the reduced collectivity compared to the original ZBM2 calculations.

## V. CONCLUSION

The lifetime measurements of the  $11/2^-$  states in mirror nuclei  $^{39}\text{Ca}$  and  $^{39}\text{K}$  were conducted by means of the recoil distance technique. By comparing our data with shell-model calculations, the enhanced  $M_p$  value was confirmed in  $^{39}\text{Ca}$ , which is ascribed to the increased proton excitations into the *fp* shell. Similarly, the enhanced  $M_n$  value was found, suggesting that the neutron cross-shell excitations are also important to understanding quadrupole transition strengths of  $^{39}\text{Ca}$ . This finding demonstrates the usefulness of lifetime measurements of analogue states in mirror nuclei as a powerful tool for probing both proton and neutron contributions to cross-shell excitations.

## ACKNOWLEDGMENTS

This work was supported by the US Department of Energy (DOE), Office of Science, Office of Nuclear Physics under Grants No. DE-SC0020451, No. DE-SC0023633 (MSU), and No. DE-AC02-06CH11357 (ANL), the National Science Foundation (NSF) under Grants No. PHY-1565546 and No. PHY-2110365, and the DOE National Nuclear Security Administration through the Nuclear Science and Security

Consortium under Award No. DE-NA0003180. This work was also supported by the German Ministry of Science and Education (BMBF) under Grant No. 5P21PKFN1. GRETINA was funded by the US DOE Office of Science. Operation of

the array at the NSCL was supported by the DOE under Grants No. DE-SC0019034 (NSCL) and No. DE-AC02-05CH11231 (LBNL). The authors would like to thank R. S. Lubna for discussions on shell-model calculations.

- [1] M. Bentley and S. Lenzi, Coulomb energy differences between high-spin states in isobaric multiplets, *Prog. Part. Nucl. Phys.* **59**, 497 (2007).
- [2] J. Ekman, C. Fahlander, and D. Rudolph, Mirror symmetry in the upper  $fp$  shell, *Mod. Phys. Lett. A* **20**, 2977 (2005).
- [3] A. M. Bernstein, V. R. Brown, and V. A. Madsen, Isospin decomposition of nuclear multipole matrix elements from  $\gamma$  decay rates of mirror transitions: Test of values obtained with hadronic probes, *Phys. Rev. Lett.* **42**, 425 (1979).
- [4] P. D. Cottle, M. Fauerbach, T. Glasmacher, R. W. Ibbotson, K. W. Kemper, B. Pritychenko, H. Scheit, and M. Steiner, The  $0_{g.s.}^+ \rightarrow 2_1^+$  transition in  $^{38}\text{Ca}$  and isospin symmetry in  $A = 38$  nuclei, *Phys. Rev. C* **60**, 031301(R) (1999).
- [5] F. M. Prados Estévez, A. M. Bruce, M. J. Taylor, H. Amro, C. W. Beausang, R. F. Casten, J. J. Ressler, C. J. Barton, C. Chandler, and G. Hammond, Isospin purity of  $T=1$  states in the  $A = 38$  nuclei studied via lifetime measurements in  $^{38}\text{K}$ , *Phys. Rev. C* **75**, 014309 (2007).
- [6] J. Henderson and S. R. Stroberg, Examination of the inversion of isobaric analogue states in mirror nuclei, *Phys. Rev. C* **102**, 031303(R) (2020).
- [7] A. Boso, S. Milne, M. Bentley, F. Recchia, S. Lenzi, D. Rudolph, M. Labiche, X. Pereira-Lopez, S. Afara, F. Ameil, T. Arici, S. Aydin, M. Axiotis, D. Barrientos, G. Benzoni, B. Birkenbach, A. Boston, H. Boston, P. Boutachkov, A. Bracco *et al.*, Isospin dependence of electromagnetic transition strengths among an isobaric triplet, *Phys. Lett. B* **797**, 134835 (2019).
- [8] K. Wimmer, W. Korten, P. Doornenbal, T. Arici, P. Aguilera, A. Algora, T. Ando, H. Baba, B. Blank, A. Boso, S. Chen, A. Corsi, P. Davies, G. de Angelis, G. de France, J.-P. Delaroche, D. T. Doherty, J. Gerl, R. Gernhäuser, M. Girod *et al.*, Shape changes in the mirror nuclei  $^{70}\text{Kr}$  and  $^{70}\text{Se}$ , *Phys. Rev. Lett.* **126**, 072501 (2021).
- [9] N. Dronchi, D. Weisshaar, B. A. Brown, A. Gade, R. J. Charity, L. G. Sobotka, K. W. Brown, W. Reviol, D. Bazin, P. J. Farris, A. M. Hill, J. Li, B. Longfellow, D. Rhodes, S. N. Paneru, S. A. Gillespie, A. Anthony, E. Rubino, and S. Biswas, Measurement of the  $B(E2 \uparrow)$  strengths of  $^{36}\text{Ca}$  and  $^{38}\text{Ca}$ , *Phys. Rev. C* **107**, 034306 (2023).
- [10] T. Beck, A. Gade, B. A. Brown, J. A. Tostevin, D. Weisshaar, D. Bazin, K. W. Brown, R. J. Charity, P. J. Farris, S. A. Gillespie, A. M. Hill, J. Li, B. Longfellow, W. Reviol, and D. Rhodes, Probing proton cross-shell excitations through the two-neutron removal from  $^{38}\text{Ca}$ , *Phys. Rev. C* **108**, L061301 (2023).
- [11] D. Morrissey, B. Sherrill, M. Steiner, A. Stolz, and I. Wiedenhoever, Commissioning the A1900 projectile fragment separator, *Nucl. Instrum. Methods Phys. Res. Sect. B* **204**, 90 (2003).
- [12] H. Iwasaki, A. Dewald, T. Braunroth, C. Fransen, D. Smalley, A. Lemasson, C. Morse, K. Whitmore, and C. Loelius, The TRIPLE PLunger for EXotic beams TRIPLEX for excited-state lifetime measurement studies on rare isotopes, *Nucl. Instrum. Methods Phys. Res. Sect. A* **806**, 123 (2016).
- [13] S. Paschalis, I. Lee, A. Macchiavelli, C. Campbell, M. Cromaz, S. Gros, J. Pavan, J. Qian, R. Clark, H. Crawford, D. Doering, P. Fallon, C. Lionberger, T. Loew, M. Petri, T. Stezelberger, S. Zimmermann, D. Radford, K. Lagergren, D. Weisshaar *et al.*, The performance of the gamma-ray energy tracking in-beam nuclear array GRETINA, *Nucl. Instrum. Methods Phys. Res. Sect. A* **709**, 44 (2013).
- [14] D. Weisshaar, D. Bazin, P. Bender, C. Campbell, F. Recchia, V. Bader, T. Baugher, J. Belarge, M. Carpenter, H. Crawford, M. Cromaz, B. Elman, P. Fallon, A. Forney, A. Gade, J. Harker, N. Kobayashi, C. Langer, T. Lauritsen, I. Lee *et al.*, The performance of the  $\gamma$ -ray tracking array GRETINA for  $\gamma$ -ray spectroscopy with fast beams of rare isotopes, *Nucl. Instrum. Methods Phys. Res. Sect. A* **847**, 187 (2017).
- [15] D. Bazin, J. Caggiano, B. Sherrill, J. Yurkon, and A. Zeller, The S800 spectrograph, *Nucl. Instrum. Methods Phys. Res. Sect. B* **204**, 629 (2003).
- [16] A. Dewald, O. Möller, and P. Petkov, Developing the recoil distance Doppler-shift technique towards a versatile tool for lifetime measurements of excited nuclear states, *Prog. Part. Nucl. Phys.* **67**, 786 (2012).
- [17] J. Chen, Nuclear data sheets for  $A = 39$ , *Nucl. Data Sheets* **149**, 1 (2018).
- [18] P. Adrich, D. Enderich, D. Miller, V. Moeller, R. Norris, K. Starosta, C. Vaman, P. Voss, and A. Dewald, A simulation tool for recoil distance method lifetime measurements at NSCL, *Nucl. Instrum. Methods Phys. Res. Sect. A* **598**, 454 (2009).
- [19] S. Agostinelli, J. Allison, K. Amako, J. Apostolakis, H. Araujo, P. Arce, M. Asai, D. Axen, S. Banerjee, G. Barrand, F. Behner, L. Bellagamba, J. Boudreau, L. Broglio, A. Brunengo, H. Burkhardt, S. Chauvie, J. Chuma, R. Chytráček, G. Cooperman *et al.*, Geant4—a simulation toolkit, *Nucl. Instrum. Methods Phys. Res. Sect. A* **506**, 250 (2003).
- [20] H. Iwasaki, A. Lemasson, C. Morse, A. Dewald, T. Braunroth, V. M. Bader, T. Baugher, D. Bazin, J. S. Berryman, C. M. Campbell, A. Gade, C. Langer, I. Y. Lee, C. Loelius, E. Lunderberg, F. Recchia, D. Smalley, S. R. Stroberg, R. Wadsworth, C. Walz *et al.*, Evolution of collectivity in  $^{72}\text{Kr}$ : Evidence for rapid shape transition, *Phys. Rev. Lett.* **112**, 142502 (2014).
- [21] C. Loelius, H. Iwasaki, B. A. Brown, M. Honma, V. M. Bader, T. Baugher, D. Bazin, J. S. Berryman, T. Braunroth, C. M. Campbell, A. Dewald, A. Gade, N. Kobayashi, C. Langer, I. Y. Lee, A. Lemasson, E. Lunderberg, C. Morse, F. Recchia, D. Smalley *et al.*, Lifetime measurement of the  $4_1^+$  state of  $^{58}\text{Ni}$  with the recoil distance method, *Phys. Rev. C* **94**, 024340 (2016).
- [22] C. Loelius, N. Kobayashi, H. Iwasaki, D. Bazin, J. Belarge, P. C. Bender, B. A. Brown, R. Elder, B. Elman, A. Gade, M. Grinder, S. Heil, A. Hufnagel, B. Longfellow, E. Lunderberg, M. Mathy, T. Otsuka, M. Petri, I. Syndikus, N. Tsunoda *et al.*, Enhanced electric dipole strength for the weakly bound states in  $^{27}\text{Ne}$ , *Phys. Rev. Lett.* **121**, 262501 (2018).

- [23] C. Morse, H. Iwasaki, A. Lemasson, A. Dewald, T. Braunroth, V. Bader, T. Baugher, D. Bazin, J. Berryman, C. Campbell, A. Gade, C. Langer, I. Lee, C. Loelius, E. Lunderberg, F. Recchia, D. Smalley, S. Stroberg, R. Wadsworth, C. Walz *et al.*, Lifetime measurement of the  $2_1^+$  state in  $^{74}\text{Rb}$  and isospin properties of quadrupole transition strengths at  $N = Z$ , *Phys. Lett. B* **787**, 198 (2018).
- [24] A. Gade, D. Weisshaar, B. A. Brown, D. Bazin, K. W. Brown, R. J. Charity, P. Farris, A. M. Hill, J. Li, B. Longfellow, D. Rhodes, W. Reviol, and J. A. Tostevin, Exploiting dissipative reactions to perform in-beam  $\gamma$ -ray spectroscopy of the neutron-deficient isotopes  $^{38,39}\text{Ca}$ , *Phys. Rev. C* **106**, 064303 (2022).
- [25] R. Elder, H. Iwasaki, J. Ash, D. Bazin, P. C. Bender, T. Braunroth, C. M. Campbell, H. L. Crawford, B. Elman, A. Gade, M. Grinder, N. Kobayashi, B. Longfellow, T. Mijatović, J. Pereira, A. Revel, D. Rhodes, and D. Weisshaar, Lifetime measurements probing collectivity in the ground-state band of  $^{32}\text{Mg}$ , *Phys. Rev. C* **104**, 024307 (2021).
- [26] W. Kessel, R. Bass, E. Hagen, N. Roberson, C. Gould, and D. Tilley, Study of excited states of  $^{39}\text{Ca}$  and  $^{39}\text{K}$ , *Nucl. Phys. A* **223**, 253 (1974).
- [27] R. S. Lubna, K. Kravvaris, S. L. Tabor, V. Tripathi, E. Rubino, and A. Volya, Evolution of the  $N = 20$  and 28 shell gaps and two-particle-two-hole states in the FSU interaction, *Phys. Rev. Res.* **2**, 043342 (2020).
- [28] E. Caurier, K. Langanke, G. Martínez-Pinedo, F. Nowacki, and P. Vogel, Shell model description of isotope shifts in calcium, *Phys. Lett. B* **522**, 240 (2001).
- [29] M. L. Bissell, J. Papuga, H. Naïdja, K. Kreim, K. Blaum, M. De Rydt, R. F. Garcia Ruiz, H. Heylen, M. Kowalska, R. Neugart, G. Neyens, W. Nörtershäuser, F. Nowacki, M. M. Rajabali, R. Sanchez, K. Sieja, and D. T. Yordanov, Proton-neutron pairing correlations in the self-conjugate nucleus  $^{38}\text{K}$  probed via a direct measurement of the isomer shift, *Phys. Rev. Lett.* **113**, 052502 (2014).
- [30] W. A. Richter, S. Mkhize, and B. A. Brown,  $sd$ -shell observables for the USDA and USDB Hamiltonians, *Phys. Rev. C* **78**, 064302 (2008).
- [31] M. Dufour and A. P. Zuker, Realistic collective nuclear hamiltonian, *Phys. Rev. C* **54**, 1641 (1996).
- [32] J. J. Valiente-Dobón, A. Poves, A. Gadea, and B. Fernández-Domínguez, Broken mirror symmetry in  $^{36}\text{S}$  and  $^{36}\text{Ca}$ , *Phys. Rev. C* **98**, 011302(R) (2018).
- [33] E. Caurier, F. Nowacki, and A. Poves, Merging of the islands of inversion at  $N = 20$  and  $N = 28$ , *Phys. Rev. C* **90**, 014302 (2014).
- [34] M. Honma, T. Otsuka, B. A. Brown, and T. Mizusaki, New effective interaction for  $pf$ -shell nuclei and its implications for the stability of the  $N = Z = 28$  closed core, *Phys. Rev. C* **69**, 034335 (2004).
- [35] J. Chen, Nuclear data sheets for  $A = 38$ , *Nucl. Data Sheets* **152**, 1 (2018).